Activation energy study of electron transport in high performance short wavelengths quantum cascade lasers

Christian Pflügl,[1,a] Laurent Diehl,[1] Arkadiy Lyakh,[2] Qi Jie Wang,[1] Richard Maulini,[2] Alexei Tsekoun,[2] C. Kumar N. Patel,[2,3] Xiaojun Wang,[4] and Federico Capasso[1,]

[1] *School of Engineering and Applied Sciences, Harvard University, Cambridge, MA 02138, USA*
[2] *Pranalytica, Inc., 1101 Colorado Ave., Santa Monica, CA 90401, USA*
[3] *Department of Physics and Astronomy, University of California, Los Angeles, CA 90095, USA*
[4] *Adtech Optics, Inc. 18007 Cortney Court, City of Industry, CA 91748,USA*
[a] *pflugl@seas.harvard.edu,*

Abstract: We present a method to study current paths through quantum cascade lasers (QCLs). The temperature dependence of the current is measured at a fixed voltage. At low temperatures we find activation energies that correspond to the energy difference between the injector ground state and the upper laser level. At higher temperatures additional paths with larger activation energies are found. Application of this method to high performance QCLs based on strained InGaAs/InAlAs quantum wells and barriers with different band-offsets allows us to identify individual parasitic current paths through the devices. The results give insight into the transport properties of quantum cascade lasers thus providing a useful tool for device optimization.

OCIS codes: (140.5965) Semiconductor lasers, quantum cascade; (250.5590) Quantum-well, -wire and -dot devices.

References and links

1. A. Lyakh, C. Pflügl, L. Diehl, Q. J. Wang, F. Capasso, X. J. Wang, J. Y. Fan, T. Tanbun-Ek, R. Maulini, A. Tsekoun, R. Go, C. Kumar, and N. Patel, "1.6 W high wall plug efficiency, continuous-wave room temperature quantum cascade laser emitting at 4.6 μm," Appl. Phys. Lett. **92**, 111110 (2008).
2. Y. Bai, S. Slivken, S. R. Darvish, and M. Razeghi, "Room temperature continuous wave operation of quantum cascade lasers with 12.5% wall plug efficiency," Appl. Phys. Lett. **93**(2), 021103 (2008).
3. A. Lyakh, R. Maulini, A. Tsekoun, R. Go, C. Pflügl, L. Diehl, Q. J. Wang, F. Capasso, and C. K. N. Patel, "3 Watt continuous-wave room temperature single-facet emission from quantum cascade lasers based on non-resonant extraction design approach," Appl. Phys. Lett. **95**(14), 141113 (2009).
4. R. Maulini, A. Lyakh, A. Tsekoun, and R. Go, C. K. N. Patel, C. Pflügl, L. Diehl, F. Capasso, "High power thermoelectrically-cooled and uncooled quantum cascade lasers with optimized reflectivity facet coatings," Appl. Phys. Lett. Appl. Phys. Lett. **95**, 151112 (2009).
5. A. Tsekoun, R. Go, M. Pushkarsky, M. Razeghi, and C. K. N. Patel, "Improved performance of quantum cascade lasers through a scalable, manufacturable epitaxial-side-down mounting process," Proc. Natl. Acad. Sci. U.S.A. **103**(13), 4831–4835 (2006).
6. J. Faist, F. Capasso, D. L. Sivco, A. L. Hutchinson, S.-N. G. Chu, and A. Y. Cho, "Short wavelength (lambda ~ 3.4 μm) quantum cascade laser based on strained compensated InGaAs/AlInAs," Appl. Phys. Lett. **72**(6), 680 (1998).
7. M. P. Semtsiv, M. Wienold, S. Dressler, W. T. Masselink, G. Fedorov, and D. Smirnov, "Intervalley carrier transfer in short-wavelength InP-based quantum-cascade laser," Appl. Phys. Lett. **93**(7), 071109 (2008).
8. W. T. Masselink, Mykhaylo P. Semtsiv, S. Dressler, M. Ziegler, M. Wienold, "Physics, growth, and performance of (In,Ga)As–AlP/InP quantum-cascade lasers emitting at l < 4 μm", phys. stat. sol. (b) 244, **8**, 2906 (2007).
9. T. Unuma, T. Takahashi, T. Noda, M. Yoshita, H. Sakaki, M. Baba, and H. Akiyama, "Effects of interface roughness and phonon scattering on intersubband absorption linewidth in a GaAs quantum well," Appl. Phys. Lett. **78**(22), 3448 (2001).
10. J. C. Shin, M. D'Souza, Z. Liu, J. Kirch, L. J. Mawst, D. Botez, I. Vurgaftman, and J. R. Meyer, "Highly temperature insensitive, deep-well 4.8 μm emitting quantum cascade semiconductor lasers," Appl. Phys. Lett. **94**(20), 201103 (2009).
11. C. G. Van de Walle, "Band lineups and deformation potentials in the model-solid theory," Phys. Rev. B **39**(3), 1871–1883 (1989).

#120415 - $15.00 USD Received 23 Nov 2009; revised 21 Dec 2009; accepted 21 Dec 2009; published 5 Jan 2010

12. H. Choi, L. Diehl, Z.-K. Wu, M. Giovannini, J. Faist, F. Capasso, and T. B. Norris, "Gain recovery dynamics and photon-driven transport in quantum cascade lasers," Phys. Rev. Lett. **100**(16), 167401 (2008).
13. R. F. Kazarinov, and R. A. Suris, "Electric and electromagnetic properties of semiconductors with superlattice," Sov. Phys. Semicond. **6**, 120 (1972).
14. C. Sirtori, F. Capasso, J. Faist, A. L. Hutchinson, D. L. Sivco, and A. Y. Cho, "Resonant Tunneling in Quantum Cascade Lasers," IEEE J. Quantum Electron. **34**(9), 1722–1729 (1998).
15. R. Terazzi, T. Gresch, A. Wittmann, and J. Faist, "Sequential resonant tunneling in quantum cascade lasers," Phys. Rev. B **78**(15), 155328 (2008).
16. A. Vasanelli, A. Leuliet, C. Sirtori, A. Wade, G. Fedorov, D. Smirnov, G. Bastard, B. Vinter, M. Giovannini, and J. Faist, "Role of elastic scattering mechanisms in GaInAs/AlInAs quantum cascade lasers," Appl. Phys. Lett. **89**(17), 172120 (2006).
17. S. Tsujino, A. Borak, E. Müller, M. Scheinert, C. V. Falub, H. Sigg, D. Grützemacher, M. Giovannini, and J. Faist, "Interface-roughness-induced broadening of intersubband electroluminescence in p-SiGe and n-GaInAs/AlInAs quantum-cascade structures," Appl. Phys. Lett. **86**(6), 062113 (2005).
18. R. Ferreira, and G. Bastard, "Evaluation of some scattering times for electrons in unbiased and biased single- and multiple-quantum-well structures," Phys. Rev. B **40**(2), 1074–1086 (1989).
19. G. Molis, A. Krotkus, and V. Vaičaitis, "Intervalley separation in the conduction band of InGaAs measured by terahertz excitation spectroscopy," Appl. Phys. Lett. **94**(9), 091104 (2009).

1. Introduction

Recently, major improvements in the performance of mid-infrared quantum cascade lasers (QCLs) were reported. Watt-level output power in continuous wave (cw) operation at room temperature with electrical-to-optical power efficiency, known as wallplug efficiency, exceeding 10% was achieved.[1,2,3,4] Several device aspects have to be considered and optimized to achieve these levels of performance. This includes bandstructure engineering and waveguide design, as well as growth and processing quality. Especially, achieving cw operation requires sophisticated processing and packaging techniques, to efficiently remove the heat dissipated. [5]

In this letter, we focus on understanding electron pathways in the bandstructure of short wavelength (~4.6μm) InGaAs/InAlAs/InP based QCLs. We have measured the temperature dependence of the current to draw conclusions on leakage paths, e. g. thermionic emission into the active region states and into the continuum and scattering into indirect valley states within the bandstructure.

1.1 Bandstructure design of short wavelength QCLs

QCLs emitting at wavelengths shorter than 5μm have transition energies larger than 250meV. The conduction band-offset of lattice matched InGaAs/InAlAs (ΔE_c= 520meV) is insufficient to design active regions with a strong confinement of the upper laser level. Growing tensilely-strained InAlAs and compressively-strained InGaAs heterostructures increases the band-offset compared to lattice matched InGaAs/InAlAs heterostructures. Emission wavelengths down to 3 μm have been reported using strained InGaAs/InAlAs and limiting factors like intervalley scattering and band-offsets for very short wavelengths were investigated.[6, 7, 8] With increasing strain the growth of the layers becomes more demanding and large band-offsets increase interface roughness scattering.[9] At the same time, the band-offset has to be large enough to suppress leakage of carriers into the continuum.[10] Therefore, it is important to choose the optimum layer compositions for any given design. To estimate the band-offset of heterostructures based on strained layers, the model-solid theory developed by van de Walle[11], which includes the effects of strain is typically used. This theory predicts reliable values for many different semiconductor heterostructures, but even for lattice matched InGaAs/InAlAs, the value obtained using this approach, 580meV, differs from the one obtained experimentally (520meV). For strain compensated structures with ~1% strain in the individual layers, this theory predicts a conduction band-offset of ~850meV, but typically smaller values (~800meV) are used for band structure simulations of these structures (see e. g. references 1, 2 and references therein). For high transition energies scattering into indirect states (X- and L- valleys) has also to be considered. These scattering mechanisms in short wavelength QCLs were already investigated[7,8] but it is very difficult to quantify these effects as the exact parameters are, like energetic position of these states, etc. are not exactly

#120415 - $15.00 USD Received 23 Nov 2009; revised 21 Dec 2009; accepted 21 Dec 2009; published 5 Jan 2010

known. This uncertainty in material parameters for active regions based on strained materials complicates significantly the evaluation and consequently the optimization of these devices.

1.2 Temperature performance of short wavelength QCLs

We designed several different structures with the goal of improving the performance of these devices for continuous wave room temperature operation. The structures were based on different active region designs including double-phonon resonance[2], non-resonant extraction designs[1,3], designs with short injector regions, and several others. For all structures we used the same composition for the InGaAs quantum wells in the active region (InAs mole fraction: 33%) corresponding to about 1% strain. Because of the different ratio of barrier to well thicknesses in the different designs and in order to achieve strain compensation by stage for all structures, different designs had different AlAs mole fractions for the InAlAs barriers in the active region (61.5%-64.2% for our structures). Despite a number of differences in the actual designs, we found a strong dependence of the high temperature performance on the AlAs mole fraction in the barrier material of the active region. Structures with lower AlAs mole fraction in general showed lower T_0 values, independent from the actual designs, which indicates that carrier leakage is a key factor limiting the high temperature performance of many structures. As QCLs are very complex structures, it is not possible to draw unambiguous conclusions about the underlying effects that caused the observed temperature performance. Therefore, we developed a method that allows the detection of parasitic current paths into the continuum in short wavelength QCLs and to verify experimentally that the strain level is optimized to suppress these parasitic paths.

To get a better understanding of the method and to verify its applicability to detect leakage current paths in the bandstructure of QCLs, we made a systematic study using two different structures that were based on the same active region layer sequence but with different strain compositions and consequently different conduction band-offsets. This ensures that other temperature dependent effects and parameters, like thermally activated backfilling, lifetimes, etc. are basically identical in both structures. The only significant difference is the electronic confinement of the states. First, we will discuss the method and the theoretical model describing our data and then show how this method can be used to detect leakage current paths through these devices.

2. Activation energy study

We investigated the temperature dependence of the current-voltage (I-V) characteristics by plotting current vs. temperature for a fixed voltage. We used mesa structures for these measurements since these devices do not lase at any temperature and voltage. This allows us to compare I-Vs from different structures without the influence of stimulated emission, which well known to lead to voltage clamping in QCLs.[12] The I-Vs were taken in pulsed operation (1% duty cycle, 125ns, 80kHz) to limit the heating of the active region.

At low temperatures, only the tunneling path from the injector ground state to the upper laser state is expected to significantly contribute to the current (see Fig. 1). Assuming only this path, the current density at a fixed voltage can be written as [13, 14, 15]

$$J = \frac{2e|\Omega|^2 \tau_\perp}{1+\Delta^2 4\tau_\perp^2 + |\Omega|^2 \tau_4 \tau_\perp} n_{inj} \exp(-\frac{\hbar\Delta}{kT}), \quad (1)$$

where e is the electronic charge, n_{inj} is the sheet carrier density in the injector, $2\hbar|\Omega|$ is the energy splitting at resonance between the injector ground state and the upper laser level (state 4), $\hbar\Delta$ is the detuning from resonance, $\tau_\perp$ and τ_4 are the dephasing time and the upper laser level lifetime, respectively. $\tau_\perp$, which is mainly determined by interface roughness scattering, is expected to depend only very weakly on the temperature and is thus assumed to be constant in our model. The upper state lifetime τ_4 is determined by both elastic and inelastic scattering. It was shown recently, that inelastic scattering rate[16, 17, 9] (alloy and interface roughness scattering) has a weight comparable to that of the optical phonons. This model does not

#120415 - $15.00 USD Received 23 Nov 2009; revised 21 Dec 2009; accepted 21 Dec 2009; published 5 Jan 2010

include the reduced injection efficiency due to electrons directly scattered from the injector states to the lower laser level and the states below this level in the active region. The scattering times for these processes are in the order of several tens of picoseconds and thus significantly longer than the upper state life time. At low applied voltages (large $\hbar\Delta$), this contribution is estimated to be a few % of the total current. At high temperatures additional current paths through energetically higher lying states in the active region states or indirect valleys, e. g. the L-valley, are expected to contribute to the current through the device (see Fig. 1). An additional current path can be described by including an additional term with an activation energy $\hbar\Delta_l$:

$$J = \frac{2e|\Omega|^2 \tau_\perp}{1+\Delta^2\tau_\perp^2+|\Omega|^2 \tau_4\tau_\perp} n_{inj} \exp(-\frac{\hbar\Delta}{kT}) + c_l(T)\exp(-\frac{\hbar\Delta_l}{kT}) \qquad (2).$$

As this path also includes electrons scattered into the continuum and indirect states, it is difficult to precisely describe the function $c_l(T)$. In this work, we used c_l and $\hbar\Delta_l$ as temperature independent fitting parameters. The deviation of this fitting curve from the one assuming only one current path (Eq. (1) is determined by $\hbar\Delta_l$. Knowledge of this second activation energy should give us insight into leakage current paths even without a model for c_l.

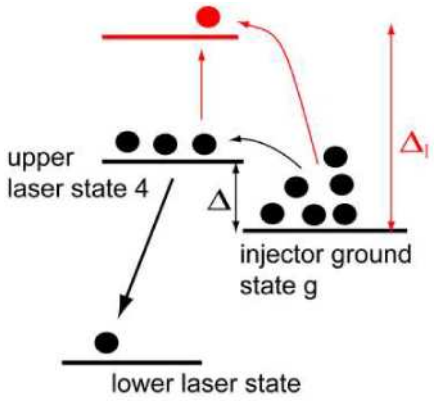

Fig. 1. Schematic diagram showing the current path from the injector ground state into the upper laser level and the transition from the upper laser level to the lower laser level (black arrows). Parasitic current paths to states above the upper laser level are indicated with red arrows. From these states the electrons can leak into the continuum as discussed in detail in the text.

3. Device fabrication and measurement techniques

The strain-compensated InGaAs/InAlAs structures were grown by metal-organic vapor phase epitaxy on InP wafers. The structures were processed into circular non-lasing wet-etched mesa devices and wet etched ridge waveguide edge emitting lasers with SiN insulation and thin gold contact layers. The mesa devices were operated in a cryostat in pulsed mode up the maximum heatsink temperature achievable in our setup (400K). The ridge devices were tested on a thermoelectric cooler and their output power was measured with a thermopile detector placed directly in front of the device facets using a gold-coated Al tube to collect the light. For low temperature measurements the lasers were also mounted in a cryostat and the measured output power was corrected for the reduced collection efficiency compared to the measurements with the detector in front of the lasers.

4. Experimental results

The two structures, S1 and S2, are based on a non-resonant extraction design and highly strained (~1%) InGaAs/AlInAs quantum wells and barriers with strain compensation in each stage.[1] The only difference between S1 and S2 is the composition of the ternaries in the

#120415 - $15.00 USD Received 23 Nov 2009; revised 21 Dec 2009; accepted 21 Dec 2009; published 5 Jan 2010

active region heterostructures. The composition was deduced from photoluminescence and x-ray measurements. The x-ray period (corresponding to the overall thickness of one cascade) is similar for both devices (S1: 45.2nm and S2: 45.5nm). From the peak in the photoluminescence (S1: 1436.1nm, S2: 1417.5 nm), we can deduce the InAs molar fraction in the InGaAs wells, which is about 67% for structure S1 and about 66% for S2. The corresponding AlAs molar fraction in the InAlAs barriers is 63.39% and 62.17% for structures S1 and S2, respectively. The van de Walle theory predicts a difference in the conduction band-offset of ~20meV between these two structures with S1 having the larger band-offset.

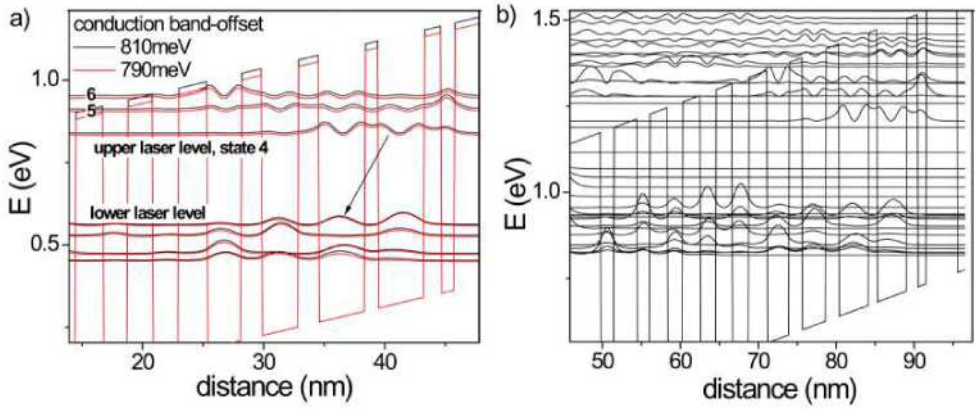

Fig. 2. a) Part of the conduction band diagram showing the most relevant active region wavefunctions (e. g. upper laser level state 4, states 5 & 6). In these calculations a conduction band-offset of 790meV (red lines) and 810meV (black lines) were used. b) shows a larger portion of the bandstructure (band-offset 790meV) including the injector and continuum states.

Although the absolute value for the bandstructure offset of these strained materials is not well known, we can still compare two structures with a band-offset difference of 20meV to estimate how the band-offset changes the wavefunctions in the active region. Figure 2 shows the active region band diagram calculated for a band-offset of 790meV and 810meV, respectively. The relative positions of the wavefunctions do not change significantly (within a few meV) for the different band-offsets. Thus, similar transition energies are expected for both structures, which is consistent with the fact that the luminescence spectra measured with S1 and S2 are essentially identical. The calculated energy spacing states 4 and 5 is about 70meV/71meV and the spacing between states 4 and 6 is ~111meV/113meV for a conduction band-offset of 790meV/810meV. Further, injection and extraction of electrons into and out of the active region and the transport through the injector miniband are expected to be comparable in both structures. The main difference is the confinement of the upper laser states 4 and the states about the upper laser level, 5 and 6, respectively. Another difference between the two samples is a slight change in energy spacing between the Γ and X/L valleys.

Figure 3(a) shows the light output – current density (L-J) characteristics of representative ridge laser devices of each structure tested in pulsed mode at room temperature. Structure S1 has larger slope efficiency and slightly lower threshold current density at room temperature compared to S2. The temperature dependence of the devices can be expressed with the characteristic temperatures T_0 and T_1. T_0 describing the temperature dependence of the threshold current density, is defined from $J_{th}(T_{in}+\Delta T)= J_{th}(T_{in})\exp(\Delta T/T_0)$, where $T_{in}+\Delta T$ is the heatsink temperature and T_{in} is the initial temperature. Similarly, the characteristic temperature for the slope efficiency, dP/dI (power over current), T_1 is defined as $dP/dI(T_{in}+\Delta T)= dP/dI(T_{in})\exp(-\Delta T/T_1)$. Both structures have a very similar characteristic temperature T_0 up to a temperature of ~300K as shown in Fig. 3(b). At higher temperatures the threshold current density of structure S2 increases faster with increasing temperature. In this temperature range, above 300K, structure S2 has also a lower value of T_1= 120K

#120415 - $15.00 USD Received 23 Nov 2009; revised 21 Dec 2009; accepted 21 Dec 2009; published 5 Jan 2010

compared to a value of 140JK for structure S1. The performance of devices S1 processed into buried heterostructures was reported in ref. 1. We obtained 1.6W continuous wave output power at room temperature with a wallplug efficiency close to 10%.[1]

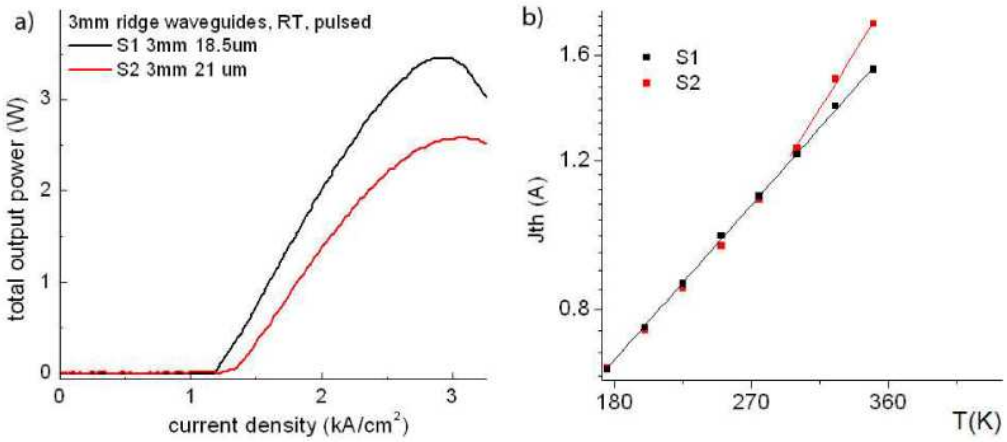

Fig. 3. a) Light-current characteristics for representative ridge laser devices of structures S1 and S2. The devices were measured in pulsed operation (125ns, 80kHz) at room temperature. The power was measured using a calibrated thermopile detector in front of the lasers. b) Threshold current densities for ridge laser devices with similar specifications as the devices shown in a) at different temperatures. For these measurements, the devices were mounted in a cryostat and cooled with liquid nitrogen. The black line shows a fit for the characteristic temperature T_0= 212T for device S1.

Figure 4 shows the measured temperature dependent currents through structures a) S1 and b) S2 for different applied voltages, 15V and 16V, below the resonance condition, which is at ~17V. The solid lines in Fig. 4(a) are fits of the experimental data with Eq. (1) (Δ and n_{inj} are the only fitting parameters) with different upper state lifetimes. The best fit was obtained by using an upper state lifetime determined by both elastic and inelastic scattering $\tau_4=(1/\tau_{4,elastic}+1/\tau_{4,inelastic}\ (T))^{-1}$ (black lines). The inelastic scattering is dominated by the temperature dependent LO-phonon scattering.[18] For our bandstructure design the calculations according to ref. 18 yield $\tau_{4,inelastic}$=1.1ps at 300K. For the elastic scattering contribution to the upper state lifetime 4 $\tau_{4,elastic}$ 1.5ps was assumed. This was estimated by adjusting the values reported for a lattice matched structure in ref. 13 for strained materials. In the case of strained materials, the alloy scattering is reduced and the interface roughness scattering increased compared to the lattice matched case. For comparison we also plotted fits assuming τ_4 to be constant with temperature (red lines), and fits assuming $\tau_4=\tau_{4,inelastic}$ to be determined only by LO-phonon scattering (blue lines) in Fig. 4(a).

#120415 - $15.00 USD Received 23 Nov 2009; revised 21 Dec 2009; accepted 21 Dec 2009; published 5 Jan 2010

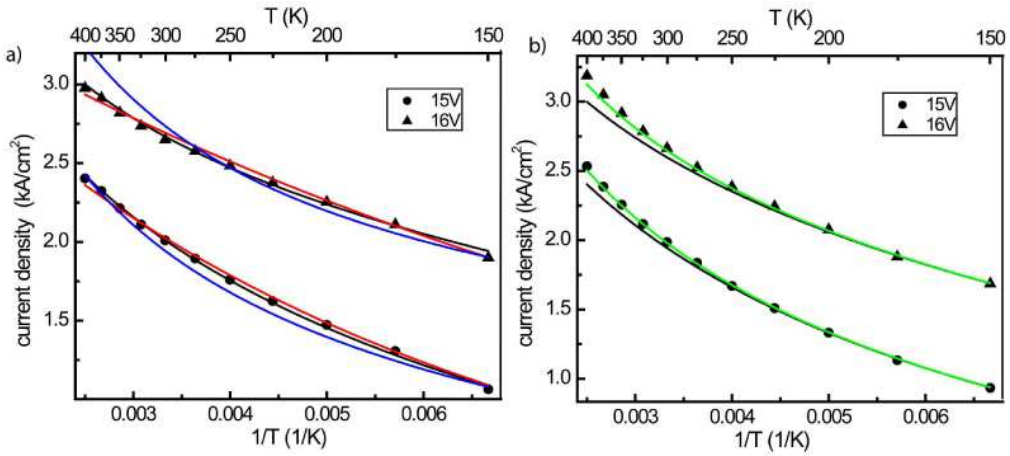

Fig. 4. Current density versus temperature characteristics for structures a) S1 and b) S2 at different applied biases. The dots and triangles show the experimental data. The black lines are fits using Eq. (1) and including elastic and inelastic contributions to the upper state lifetime τ_4. In a) the red lines are fits using a temperature independent upper state lifetime τ_4 and the blue lines are fits using τ_4 including only inelastic LO-phonon scattering. In b) the green lines include a second current path with an activation energy Δ_1 according to Eq. (2).

The fits with a lifetime including elastic and inelastic scattering give the best agreement with the experimental results. From these fits we are able to obtain Δ for a given voltage, shown in Table 1. The numbers correspond very well to the calculated energy differences between the injector ground and the upper laser state. For the sheet carrier density, we obtained $4.7*10^{10}$ cm^{-2} and $4*10^{10}$ cm^{-2} for 15V and 16V, respectively, which is close to the expected value according to the nominal doping, $6*10^{10}$ cm^{-2}. The small difference between the two values at different voltages are likely due to the smaller injection efficiency at lower applied voltages, caused by scattering of electrons from the injector states directly into the lower states in the active region. In the case of structure S2, we could not get a good fit using Eq. (1) over the whole temperature range. Therefore, we fitted only the low temperature data with Eq. (1) (black lines in Fig. 4(b)), which allowed us to obtain $\hbar\Delta$ (Table 1). The values for $\hbar\Delta$ and n_{inj} are similar to the ones obtained for structure S1.

The high temperature data of structure S2 can be fitted by using Eq. (2). This fit gives a second activation energy $\hbar\Delta_1$=90meV(±25meV)+$\hbar\Delta$ (see green lines in Fig. 4(b)). As the error bar for this fit is rather large it is very likely that several current paths contribute to the observed leakage current in this structure compared to structure S1. Based on the energy range of $\hbar\Delta_1$, the leakage current can be attributed to electrons directly injected into state 6 ($\hbar\Delta_1$=110meV+$\hbar\Delta$) or into state 5 ($\hbar\Delta_1$=70meV+$\hbar\Delta$), from where electrons can easily scatter into state 6. Because of the lower barrier height in structure S2 as compared to structure S1, state 6 is not well confined and carriers injected and scattered into this state can escape into the continuum. Other leakage current paths include electrons that are injected into state 4 and subsequently transferred to states 5 and 6 or directly to continuum states by thermionic emission. Electrons can also be scattered into indirect states (X- and L- valleys). However, we assume this current path to be small in view of recent experimental data, which shows that the energy spacing between Γ and X/L valleys is larger than previously expected.[19]

From our data we cannot definitely rule out leakage into the continuum or indirect states in structure S1. Therefore, the data for an additional structure with even higher band offset would be necessary. Nevertheless, the I-V characterization method presented in the paper allowed us to understand the origin of the difference in device performance between structures S1 and S2. This is particularly important in the optimization process of complex QCL structures, as differences in device performance can have many different reasons, including growth and processing quality.

#120415 - $15.00 USD Received 23 Nov 2009; revised 21 Dec 2009; accepted 21 Dec 2009; published 5 Jan 2010

Table 1. Activation energy [a)]

	ħΔ (meV) S1	ħΔ (meV) S2	Calculated ħΔ (meV)
16V	6	9	10
15V	14	17	18

[a)]Activation energy deduced from the low temperature data (150K-250K) shown in Fig. 4 for the structures S1 and S2 at different applied biases (15V and 16V, see first column) and calculated energy difference between the injector ground state and the upper laser level. The quasi Fermi energy in the injector ground state is 4meV, assuming all electrons to be in this state. For the calculation a conduction band-offset of 790 meV was assumed.

5. Conclusion

In conclusion, we presented a method to investigate leakage current paths through the bandstructure of QCLs. This is especially useful if one works with new material systems or systems with high strain, where the band-offsets are not accurately known. Although the band-offsets cannot be deduced directly, this method provides important information that helps to optimize material composition for a certain active region design.

The presented results obtained with two similar structures are important to show the applicability of this method to detect current paths. Future work will include a systematic study of a set of structures with varying energy spacing of the active region states to gain further insight into the different current paths contributing to the overall current.

Acknowledgements

This work was supported in part through a DARPA Contract No. W911QX-07-C-0041 (Approved for Public Release, Distribution Unlimited). Part of the processing work was performed at the Center for Nanoscale Systems (CNS), a member of the National Nanotechnology Infrastructure Network (NNIN), which is supported by the National Science Foundation under NSF award no. ECS-0335765.

#120415 - $15.00 USD Received 23 Nov 2009; revised 21 Dec 2009; accepted 21 Dec 2009; published 5 Jan 2010